

# All-optical GeV electron bunch generation in a laser-plasma accelerator via truncated-channel injection

A. Picksley,<sup>1,\*</sup> J. Chappell,<sup>1</sup> E. Archer,<sup>1</sup> N. Bourgeois,<sup>2</sup> J. Cowley,<sup>1</sup> D. R. Emerson,<sup>3</sup> L. Feder,<sup>1</sup> X. J. Gu,<sup>3</sup> O. Jakobsson,<sup>1</sup> A. J. Ross,<sup>1</sup> W. Wang,<sup>1</sup> R. Walczak,<sup>1,4</sup> and S. M. Hooker<sup>1</sup>

<sup>1</sup>*John Adams Institute for Accelerator Science and Department of Physics, University of Oxford, Denys Wilkinson Building, Keble Road, Oxford OX1 3RH, United Kingdom*

<sup>2</sup>*Central Laser Facility, STFC Rutherford Appleton Laboratory, Didcot OX11 0QX, United Kingdom*

<sup>3</sup>*Scientific Computing Department, STFC Daresbury Laboratory, Warrington WA4 4AD, United Kingdom*

<sup>4</sup>*Somerville College, Woodstock Road, Oxford OX2 6HD, United Kingdom*

(Dated: July 26, 2023)

We describe a simple scheme, truncated-channel injection, to inject electrons directly into the wakefield driven by a drive pulse guided by an all-optical plasma channel. We use this approach to generate dark-current-free 1.2 GeV, 4.5% relative energy spread electron bunches with 120 TW laser pulses guided in a 110 mm-long hydrodynamic optical-field-ionized (HOFI) plasma channel. Our experiments and particle-in-cell simulations show that high-quality electron bunches were only obtained when the drive pulse was closely aligned with the channel axis, and was focused close to the density down-ramp formed at the channel entrance. Start-to-end simulations of the channel formation, and electron injection and acceleration show that increasing the channel length to 410 mm would yield 3.65 GeV bunches, with a slice energy spread  $\sim 5 \times 10^{-4}$ .

In the last 15 years it has become well established that laser-driven plasma accelerators [1] can accelerate few-femtosecond [2–6] electron bunches to GeV-scale energies in accelerator stages only a few centimetres long [7–13]. These highly desirable features make laser-plasma accelerators attractive for driving compact, femtosecond-duration light sources [14, 15], including free-electron lasers (FELs). Indeed, FEL gain has recently been reported in experiments utilizing laser- [16, 17] and beam-driven [18, 19] plasma accelerators. Other work has demonstrated generation of incoherent soft x-radiation in an undulator [20], and at photon energies in the keV range [21] from betatron oscillations in the plasma accelerator itself, and at MeV energies from Thomson scattering [22–24].

The most demanding applications of laser-plasma accelerators, such as driving short-wavelength FELs, require the generation of multi-GeV electron bunches with high peak current, low transverse emittance, and small shot-to-shot jitter of the bunch properties. For these applications it is preferable to operate in the linear, or quasi-linear, regime [25] in order to prevent uncontrolled self-injection at one or more points along the length of the accelerator. However, this regime brings two significant challenges. First, relativistic self-focusing does not occur and hence the drive laser pulse must be guided over the tens to hundreds of Rayleigh ranges required to reach multi-GeV energies. Second, trapping of electrons in the plasma wave is more difficult since the electric fields of the plasma wave are lower than in the highly nonlinear regime [25].

In order to meet the first of these challenges, we have developed low-density hydrodynamic optical-field-ionized (HOFI) plasma channels [26–29], building on

pioneering work by Milchberg et al. [30–33]. These channels have low losses, and could in principle be several metres long [34]. Experiments have demonstrated guiding of relativistically-intense laser pulses through 200 mm-long plasma channels with axial densities as low as  $1 \times 10^{17} \text{ cm}^{-3}$  [34–37], and operation at kHz pulse repetition rates [38].

In this paper we demonstrate a new approach that can address both challenges in a single stage. We show that the density down-ramp formed at the start of a HOFI channel can promote electron injection directly into the quasi-linear wakefield driven by a channel-guided drive pulse. We demonstrate experimentally that this truncated-channel injection (TCI) scheme produces electron bunches with an energy up to 1.2 GeV, and a root-mean-square (rms) energy spread of  $\sigma_E/\mu_E = 4.5\%$  from 120 TW (5.8 J, 50 fs) laser pulses guided in 110-mm-long HOFI channels. We show that these high-quality TCI bunches are only generated when the drive laser is: (i) focused close to the down-ramp at the channel entrance; and (ii) well-aligned with, and hence guided by, the HOFI channel. In contrast, we find that bunches produced by ionization injection have much larger energy spread and are generated preferentially when the drive pulse is mis-aligned with the channel. The experimental results are found to be in excellent agreement with start-to-end simulations of the complete TCI scheme, which includes hydrodynamic simulations of the formation of the HOFI channel, high-resolution particle-in-cell (PIC) simulations of the electron injection, and boosted-frame PIC simulations of the accelerator stage. These simulations show that dephasing was not reached in our experiments, and that extending the channel length to the dephasing length  $L_d \approx 410 \text{ mm}$  would yield electron bunches of en-

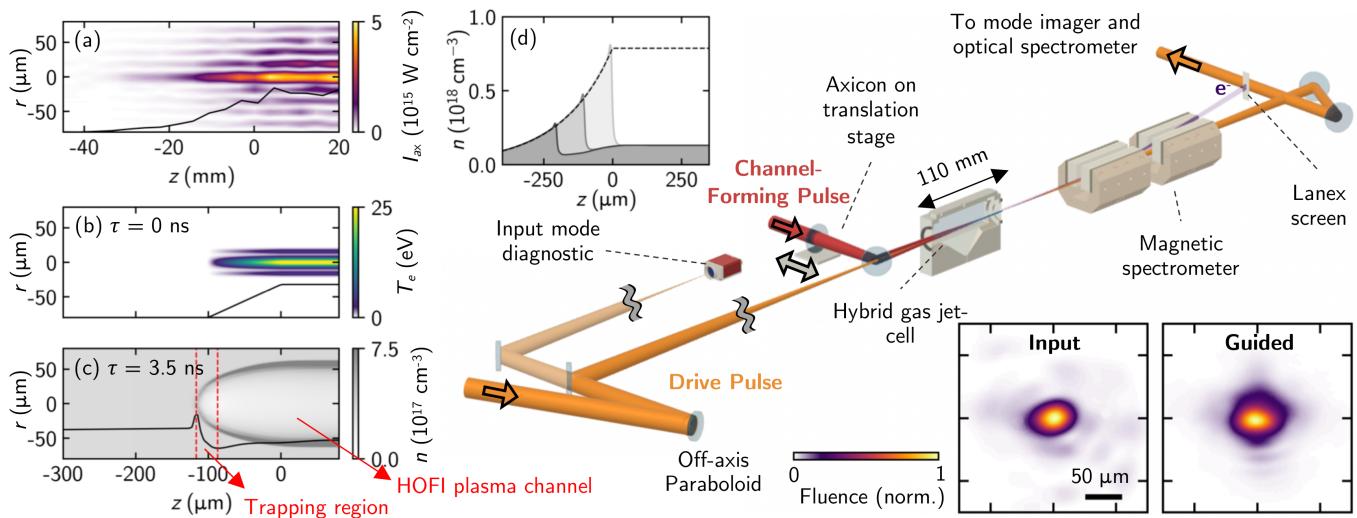


Figure 1. Schematic of truncated-channel injection scheme. The main figure shows how the driving (orange) and channel-forming (red) laser pulses were coupled into a hybrid gas jet-cell, and the configuration of the far-field input, exit mode, and electron diagnostics. Left inset: (a) Measured axicon longitudinal intensity profile, (b) calculated initial electron temperature profile, and (c) calculated density profile of the truncated HOFI plasma channel 3.5 ns after arrival of the channel-forming pulse. In each panel, the black curve shows the relative magnitude of each variable along the optical axis. (d) Results of fluid simulations of the longitudinal variation of the total density  $n = n_e + n_H$  for three simulations with  $T_e(r, z - \delta z)$  with  $\delta z = 0, -100, -200 \mu\text{m}$ . Right inset: Measured transverse fluence profiles of the drive laser at focus and at the exit of the HOFI channel.

ergy 3.65 GeV, a slice energy spread below the per-mille level, a peak current of 0.8 kA, and a normalized transverse emittance of  $\epsilon_{\perp} < 5 \text{ mm mrad}$ . These properties appear to be well matched to the requirements of soft X-ray FELs driven by 100 TW class lasers.

Before describing this work in detail we note that Scott et al. [39] have investigated electron injection in plasma structures generated by a laser prepulse; these had a similar transverse shape to those we investigate here, but were much shorter ( $\sim 100 \mu\text{m}$ ) and were not coupled to a guiding structure. Several groups have recently investigated GeV-scale electron acceleration in all-optical plasma channels. Oubriere et al. used 40 TW laser pulses to generate  $\sim 50 \text{ pC}$ , 1.1 GeV bunches with relative energy spread 4%, following blade-induced shock injection in a 15-mm-long all-optical channel generated with an axiparabola [40]. Miao et al. used 300 TW laser pulses to generate electron beams with large energy spreads, and a central energy peaking at  $\sim 5 \text{ GeV}$  following ionization injection in nitrogen-doped, 20-cm-long HOFI channels [41]. Very recent work investigating electron injection via density transitions generated by hydrodynamically-expanding shocks has demonstrated it as a feasible injection scheme for plasma-based [42] and laser-based [43] acceleration.

Figure 1 outlines the TCI scheme, and the experimental arrangement employed. Our experiments were undertaken with the Astra-Gemini TA3 Ti:sapphire laser at the Rutherford Appleton Laboratory, which delivered two independent beams with central wavelength  $\lambda_0 = 800 \text{ nm}$

and full-width at half-maximum (FWHM) durations of  $(47 \pm 3) \text{ fs}$ .

The channel-forming beam, of pulse energy  $(86 \pm 17) \text{ mJ}$ , was focused by an axicon lens to form an initial plasma column within the 110-mm-long gas target. The drive beam, of pulse energy  $(5.8 \pm 0.2) \text{ J}$ , was focused into the gas target by an off-axis paraboloid, used at  $f/40$ , to form a focus of spot size ( $1/e^2$  intensity radius)  $w_0 \approx 40 \mu\text{m}$ . The Rayleigh range and peak intensity of the drive pulse were determined to be  $z_R \approx 6 \text{ mm}$  and  $I_{\text{pk}} \approx 2.4 \times 10^{18} \text{ W cm}^{-2}$  ( $a_0 \approx 1.0$ ) respectively. The delay between the arrival of the two pulses was set to  $\Delta\tau = 3.5 \text{ ns}$ . A small fraction ( $< 1\%$ ) of the beam was transmitted through the final turning mirror and brought to focus in order to measure the transverse offset,  $\delta r$ , of the drive pulse focus relative to the axis of the plasma channel on-shot.

The target comprised a 110 mm long hybrid gas jet-cell [44]. The drive and channel-forming beams were coupled in and out of this via 6 mm diameter ceramic pinholes at the entrance and exit of the cell. A 2% mix of nitrogen in hydrogen was pulsed into the cell. Fluid simulations [45] indicated that the rms variation of the gas density along the cell axis was  $< 3\%$  inside the cell, and that beyond the pinholes the atomic density decreased by a factor of  $e$  in a distance of 4.2 mm (i.e.  $< z_R$ ).

After leaving the cell the drive laser pulse was reduced in intensity by reflection from an optical wedge and imaged by an achromatic Keplerian telescope onto a 16-bit CMOS detector and two fiber-based optical

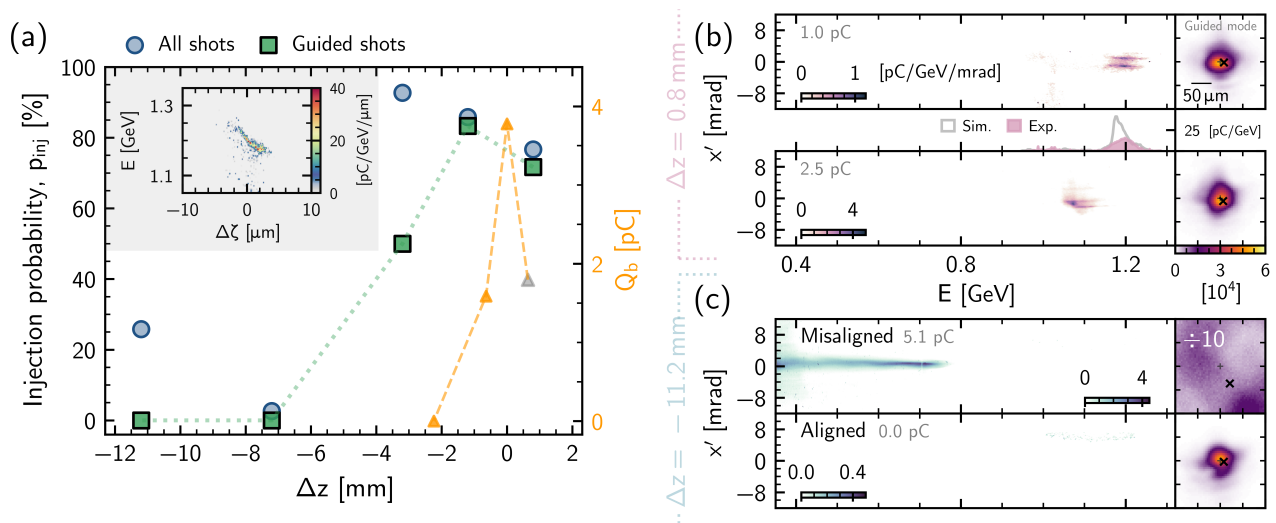


Figure 2. (a) Left axis: Measured injection probability,  $p_{inj}$ , as a function of  $\Delta z = z_{ch} - z_f$  for all (grey circles) and well guided (green squares) shots. Right axis: Variation with  $\Delta z$  of the trapped electron bunch charge,  $Q_b$ , at the end of the HOFI channel calculated from PIC simulations. Inset (grey): PIC calculation of the longitudinal phase space distribution of the injected electron bunch at the channel exit for  $\Delta z = 0.8$  mm, indicated by the grey data point. This simulation is used in comparison to experimental measurements throughout the study. (b) Two examples of the measured, angularly-resolved, electron energy distributions (left), and the corresponding exit modes (right) of the guided drive beam for  $\Delta z = 0.8$  mm. The black cross shows the drive input position. Below the upper plot is shown a comparison between the measured and simulated angularly-integrated electron energy spectra. (c) Plots as in (b), but for  $\Delta z = -11.2$  mm: The upper plot shows an example of the high charge, but large energy spread beams that are observed with a large input offset ( $\delta r = 50$   $\mu$ m). The lower plot shows an example of the high-quality guiding, but lack of electron injection, that is observed for well-aligned beams ( $\delta r = 10$   $\mu$ m).

spectrometers. The electron energy spectrum was measured by an electron spectrometer comprising two 30 cm-long,  $(1.01 \pm 0.01)$  T dipole magnets and two scintillating screens imaged onto 16-bit CMOS detectors [45].

Truncating the plasma channel was achieved by translating the axicon along its optical axis to vary the longitudinal position of the start of the HOFI plasma channel. In principle the start of the channel can be calculated from the diameter (26 mm) of the central hole in the axicon and the approach angle of the axicon ( $1.6^\circ$ ). In practice, however, the characteristic length over which the intensity of the line focus increases from zero is determined by the wavefront uniformity of the collimated beam, diffraction, and alignment of the axicon to the beam. Figure 1(a) shows the measured intensity distribution,  $I_{ax}(r, z)$ , near the start of the axicon line focus, and Fig. 1(b) shows the calculated 2D electron temperature profile  $T_e(r, z)$  of the resulting initial plasma column [45]. It can be seen that the strong intensity dependence of optical field ionization causes the onset of the plasma column to be significantly sharper than that of  $I_{ax}(r, z)$ . The body of this initial plasma column expands radially, driving a cylindrical shock into the surrounding gas, to form a HOFI channel. During this expansion a collar of neutral gas builds up on the outer surface of the shock front [34, 37], which is ionized by the drive pulse as it propagates, to form a deep, low-loss conditioned HOFI (CHOFI) channel [34, 36].

As shown in Fig. 1(c), hydrodynamic simulations show that the front edge of the initial plasma column expands longitudinally to form a hemispherical acoustic shock wave; the expansion of the electron density and neutral density ( $n = n_e + n_H$ ) along the laser axis resembles a Sedov-Taylor-like *spherical* expansion for the times simulated (0 ns to 5 ns) [45, 46], leading to a lower shock height than that formed by the *radial* expansion that occurs in the main part of the channel. We note that the leading edge of the drive laser will ionize any neutral atoms, to give a new electron density equal to  $n$ . The scale length of the transition,  $\hat{L}_{tr} = n_{e0}/(dn_e/dz)$ , where  $n_{e0}$  is the axial density in the main part of the HOFI channel can be varied by adjusting the relative position of the start of the axicon focus  $z_{ch}$  and the plume of gas exiting the cell entrance. Fig. 1(d) shows the longitudinal density profile  $n(z)$  calculated for a fixed initial gas density distribution and  $T_e(r, z - \delta z)$ , with  $\delta z = 0, -100, -200$   $\mu$ m where  $T_e(r, z)$  is shown in Fig. 1(b). The black dashed line indicates  $n_{gas}$  at  $\tau = 0$ . It can be seen that the ramp length is  $\approx 70$   $\mu$ m and the ratio of the peak shock density to the on-axis density in the main part of the channel,  $n_{shock}/n_{e0}$  can be varied from approximately 2 to 6, corresponding to a variation of  $\hat{L}_{tr} = 70$   $\mu$ m to 15  $\mu$ m. These scale lengths are short compared to the plasma wavelength  $\lambda_p = 2\pi c(n_{e0}e^2/m_e\epsilon_0)^{-1/2} \approx 100$   $\mu$ m, and hence injection is expected to occur as a result of the abrupt change in wakefield phase as the plasma electrons cross

the density transition [47–49], rather than a result of the decrease in wake velocity that occurs for long ( $\hat{L}_{\text{tr}} \gg \lambda_p$ ) density transitions [50].

We examined the TCI scheme by setting the longitudinal position,  $z_f$ , of the drive pulse focus to coincide with the position of the front pinhole, and varying  $z_{\text{ch}}$ . Their separation,  $\Delta z = z_{\text{ch}} - z_f$ , was varied between  $-11.2$  mm and  $0.8$  mm. We note that in a standard guiding experiment  $\Delta z \ll 0$  mm, so that the entrance to the channel is far upstream of the drive pulse focus. The on-axis plasma density of the channel was set to a low value,  $\sim (1.3 \pm 0.1) \times 10^{17} \text{ cm}^{-3}$ , so that ionisation injection was not observed for well-guided pulses in a standard guiding geometry ( $\Delta z = -11.2$  mm), defined using limits on the measured spot size and average fluence of the light imaged at the exit of the plasma channel [45].

Figure 2(a) shows the recorded injection probability,  $p_{\text{inj}}$ , as a function of  $\Delta z$ , where injection is considered to have occurred if the total charge recorded by the electron spectrometer was above  $0.05$  pC. For well-guided shots, electron bunches were observed for  $-3.2 \text{ mm} \leq \Delta z \leq 0.8 \text{ mm}$ , i.e. when the the drive focus was well within  $z_R$  of the leading edge of the plasma channel. The injection success rate for 124 well-guided shots with  $\Delta z \geq -3.2$  mm was 74%. In contrast, no electron injection was observed in 73 well-guided shots when  $\Delta z \leq -7.2$  mm.

With the channel entrance at its most downstream position,  $\Delta z = 0.8$  mm, high-quality guiding and electron acceleration could be observed simultaneously when the input beam was well aligned with the HOFI channel, as shown in Fig. 2(b). Electron bunches of pC-scale charge with mean energies in excess of  $1$  GeV and few-percent energy spreads were consistently observed for input offsets  $\delta r \lesssim 10 \mu\text{m}$ . In contrast, as shown in the lower panel of Fig. 2(c), electron injection was not observed for well guided shots when the channel entrance was located upstream of the drive pulse focus ( $\Delta z \leq -7.2$  mm). In this configuration, injection was only observed when the drive pulse was offset transversely from the channel axis, an example of which is shown in the upper panel of Fig. 2(c).

The spectral shift of the drive pulses provides insight into wakefield excitation along the plasma channel. Figure 3(a) shows, as a function of  $\delta r$ , the intensity-weighted average wavelength,  $\langle \lambda \rangle$ , of the transmitted drive pulse, together with a measure of the wavelength shift,  $\delta \langle \lambda \rangle = \langle \lambda \rangle / \lambda_0$ . It can be seen that well-aligned shots ( $\delta r \lesssim 30 \mu\text{m}$ ) are strongly correlated with high transmission and significant red-shifting, corresponding to good guiding and strong wakefield excitation. In contrast, shots with large  $\delta r$  are strongly associated with low transmission and significant blue-shifting, consistent with significant ionization by the drive pulse.

Figures 3(b) and (c) show corresponding effects in the measured electron energies, with larger mean energies  $\mu_E$  measured for smaller  $\delta r$ . As shown in Fig. 3(c),

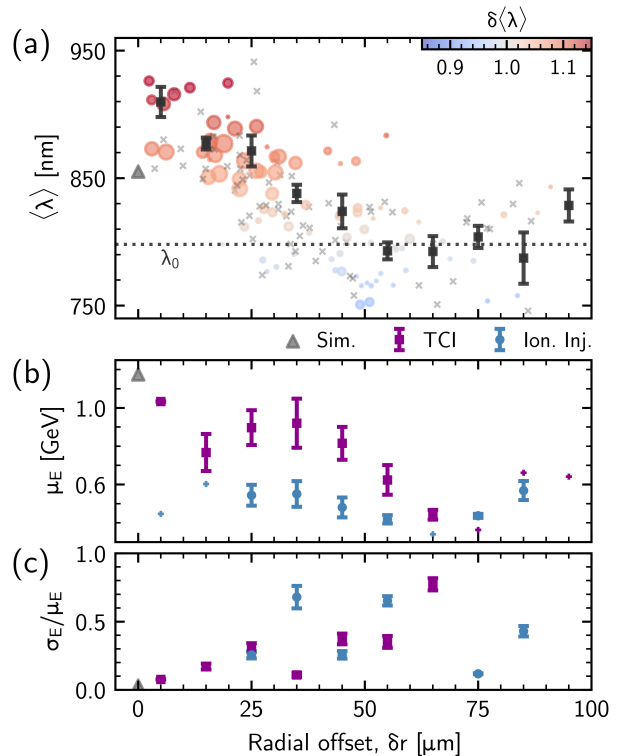


Figure 3. Variation with  $\delta r$  of the spectra of the output drive and electron beams. (a) Intensity-weighted average wavelength,  $\langle \lambda \rangle$ , of the drive pulses for  $\Delta z = 0.8$  mm. The size of data points corresponds to the relative fluence of the measured guided mode; grey crosses represent shots that were not guided. Black squares show binned averages of guided shots (see below). The grey triangle shows the result obtained from the PIC simulation for  $\Delta z = 0.8$  mm. (b) Mean bunch energy  $\mu_E$  for guided shots [45] for TCI (purple squares) and ionisation injection (blue circles); bins containing only a single event are shown by ‘+’ markers. For the ionisation injection dataset,  $\Delta z = -11.2$  mm and  $n_{e0} = (2.2 \pm 0.1) \times 10^{17} \text{ cm}^{-3}$ . (c) Ratio of the average rms energy spread  $\sigma_E$  of electron bunches to  $\mu_E$ . For all plots the data points with error bars are averages over  $10 \mu\text{m}$ -wide bins, with the error bars showing one standard error.

very well aligned shots ( $\delta r \leq 10 \mu\text{m}$ ) have dramatically lower relative rms energy spread —  $\sigma_E / \mu_E \approx 7\%$  on average, with a best of  $4.5\%$  — than less well aligned shots. Furthermore, these well aligned shots exhibited percent-level energy stability, with a mean energy of  $\mu_E = (1.033 \pm 0.010) \text{ GeV}$ .

For larger input offsets ( $10 < \delta r \leq 50 \mu\text{m}$ ), electron bunches of higher charge ( $\sim 10$  pC) were obtained, but their spectra typically comprised multiple peaks superposed on a continuous spectrum extending up to  $\sim 1.0$  GeV, with a mean energy  $\mu_E \sim 0.8$  GeV. For very large offsets ( $\delta r > 50 \mu\text{m}$ ), strong blue-shifting of the drive pulse was observed, and the electron spectra were effectively continuous, with  $\mu_E \sim 0.5$  GeV.

Figures 3(b) and (c) also show results for the case

of ionization injection from the nitrogen dopant, which was studied by increasing the on-axis density to  $n_{e0} = (2.2 \pm 0.1) \times 10^{17} \text{ cm}^{-3}$  and shifting the axicon to  $\Delta z = -11.2 \text{ mm}$ , to suppress injection via TCI. It is noticeable that  $\mu_E$  is lower, and much less sensitive to  $\delta r$ , for ionisation injection. It was also observed that, with ionization injection, electrons were preferentially injected when the drive pulse was slightly mis-aligned with respect to the axis of the channel; injection occurred only twice in 26 shots with  $\delta r \leq 20 \mu\text{m}$  ( $\sim 7\%$ ) but occurred in  $\sim 30\%$  of well-guided events for  $20 < \delta r \leq 50 \mu\text{m}$ .

The data presented in Figs 2 and 3 may be interpreted as follows. At the lower density investigated in this work, high quality electron injection only occurred when the drive pulses were: (i) well aligned with the channel ( $\delta r < 10 \mu\text{m}$ ); and (ii) focused close to the channel entrance ( $\Delta z = 0.8 \text{ mm}$ ). For these conditions, the drive pulse was strongly red-shifted, consistent with strong wake excitation, and  $\sim 1 \text{ GeV}$  electron bunches with few-percent energy spread were injected and accelerated with an injection probability of  $\sim 80\%$ . When the channel entrance was located far upstream of the drive focus, electron bunches were only generated if the drive pulse was mis-aligned; in this case, the electron spectra were broad-band, and the transmitted drive pulses had low energy transmission and were less strongly red-shifted, or even blue-shifted. These observations are consistent with poorly-aligned drive pulses interacting with the higher-density channel walls and surrounding neutral gas, triggering uncontrolled electron injection, potentially at several points along the channel. For the case of ionization injection, broad-band electron bunches were generated for a wide range of  $\delta r$ , suggesting that high-quality guiding was not necessary, and that injection occurred at several points along the plasma channel.

To gain further insight we performed start-to-end modelling of the channel formation and electron acceleration process. The chain of codes employed is described in detail in [45], but, briefly was as follows. First, the particle-in-cell (PIC) code EPOCH [51] was used to calculate the initial electron temperature distribution  $T_e(r, z)$  [see Fig. 1(b)] from  $I_{\text{ax}}(r, z)$ . Second, the Eulerian code FLASH [52] was used to perform three-dimensional hydrodynamic simulations of the evolution of the truncated plasma column up to the arrival time of the drive pulse, using  $T_e(r, z)$  and the initial longitudinal gas density distribution obtained from fluid modelling of the hybrid cell-jet. Third, propagation of the drive pulse through the plasma channel was calculated with the PIC code FBPIC [53] in two stages: (i) electron bunch generation and trapping at the down-ramp was calculated by a high-resolution simulation in the lab-frame; then (ii) this bunch was input into a boosted-frame simulation to calculate acceleration over the remainder of the channel. An Airy-like drive laser focus with  $\delta r = 0$  and other parameters similar to the experiment was assumed.

The right-hand axis of Fig. 2(a) shows the calculated electron bunch charge  $Q_b$  at the channel exit for several values of  $\Delta z$ . It can be seen that the variation of  $Q_b$  with  $\Delta z$  is qualitatively similar to that of the measured  $p_{\text{inj}}$ , although the range of  $\Delta z$  for which injection is observed in the simulations is smaller. The inset to this figure shows the calculated longitudinal phase space of the bunch at the exit of the channel for  $\Delta z = 0.8 \text{ mm}$ . The properties of this bunch are:  $\mu_E = 1.175 \text{ GeV}$ ,  $\sigma_E = 38 \text{ MeV}$  (3.2%), and  $Q_b = 1.8 \text{ pC}$ . The calculated FWHM bunch duration was  $9.4 \text{ fs}$ , and the mean slice energy spread was  $(1.0 \pm 0.4)\%$ . The average accelerating gradient experienced by the bunch was approximately  $11 \text{ GV m}^{-1}$ . The spectra of the electron bunch and the transmitted drive pulse are found to be in good agreement with the measurements, as evident in Figs 2(b) and 3(a).

Simulations showed that efficient coupling of the drive pulse and electron bunch into the HOFI channel depended on  $w_0$  and  $z_f$ . For the conditions of Fig. 2, approximately 20% of the trapped charge was coupled into the channel, the rest being immediately dephased and ejected from the wakefield. Improper matching of the drive into the HOFI channel was found to have a deleterious effect on the bunch properties since poor matching results in rapid spot-size oscillations, which in turn leads to transverse ejection of particles from the wakefield with each oscillation. These effects are evident in Fig. 4(a), which shows the evolution with  $z$  of the mode size and trapped charge for the same channel parameters as Fig. 2 and several Airy input modes mismatched to the channel by  $\Delta = w_m - w_0$ . It can also be seen that for a matched Gaussian mode  $> 40\%$  of injected bunch charge is transported into the channel, increasing the peak current by an order of magnitude compared to the Airy mode.

Figure 4 also shows the evolution of the bunch characteristics for longer channels than investigated experimentally, i.e. up to the dephasing length  $L_d \approx 410 \text{ mm}$ . At  $z = L_d$  the properties of the bunch are found to be:  $\mu_E = 3.65 \text{ GeV}$ ;  $\sigma_E = 487 \text{ MeV}$  ( $\sigma_E/\mu_E = 13.3\%$ ); an rms duration of  $\sim 26 \text{ fs}$ , corresponding to a peak current  $I_{\text{peak}} \approx 0.8 \text{ kA}$ ; and a normalized projected transverse emittance of  $\epsilon_{n,\perp} \approx 5.8 \text{ mm mrad}$  (with a slice-average of  $\epsilon_{n,\perp}^{\text{slice}} \approx 3.6 \text{ mm mrad}$ ).

The bunch exhibits negative chirp  $h = -1.2 \text{ MeV fs}^{-1}$  immediately after injection (as in [54]), but the chirp increases with acceleration to positive values, becoming  $h = 49 \text{ MeV fs}^{-1}$  at  $z = L_d$ . We note that, thanks to the linear longitudinal phase-space, a plasma-based dechirper [55] could be used to reduce  $\sigma_E$  to the level of the slice-averaged energy spread,  $\sigma_E^{\text{slice}}/\mu_E \sim 5 \times 10^{-4}$ , resulting in electron bunches that appear to be well-suited to driving a compact FEL. In the 1D limit, three conditions must be satisfied [56]: (i)  $\sigma_E/\mu_E < \rho$ ; (ii)  $L_g = \lambda_u/4\pi\sqrt{3}\pi\rho < z_R \approx \pi\sigma_r^2/\lambda_R$ ; and (iii)  $\epsilon_{\perp} = \epsilon_{n,\perp}^{\text{slice}}/\gamma < \lambda_R/4\pi$ . Here  $\rho$  is the Pierce parameter,  $L_g$

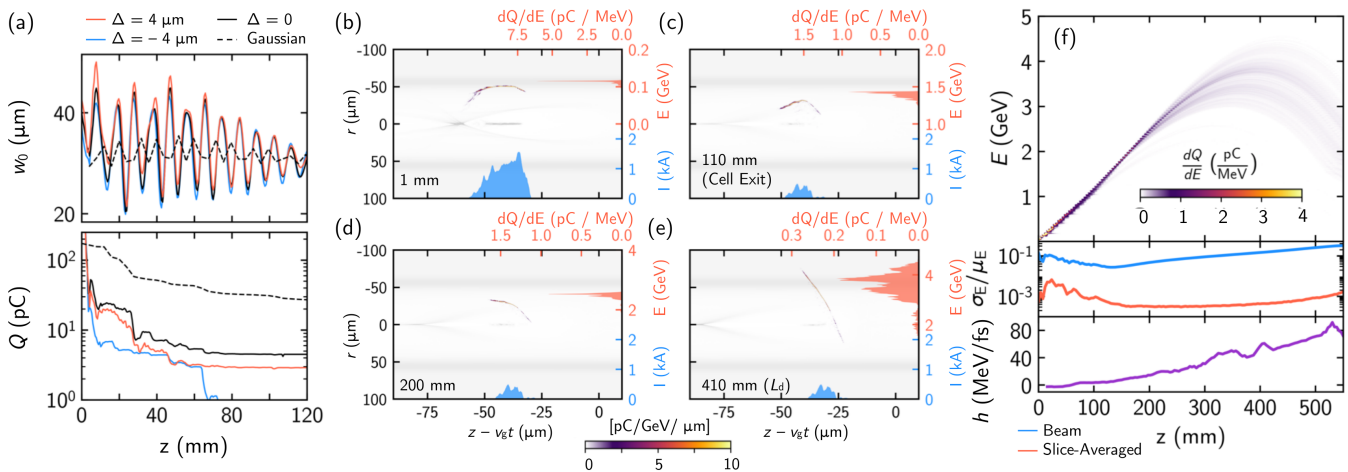


Figure 4. (a) Laser spot size (top) and TCI bunch charge (bottom) during propagation for input modes of different sizes. (b)-(e) Longitudinal phase space of the beam injected via TCI at  $z = 1 \text{ mm}$ ,  $110 \text{ mm}$  (exit of cell),  $200 \text{ mm}$ , and  $410 \text{ mm}$  (one dephasing length) respectively. The electron density profile is shown overlaid grey. Also shown is the beam energy distribution (red) and current profile (blue). (f) Evolution of the properties of the TCI-injected bunch during propagation, showing the relative energy spread of the beam ( $\sigma_E/\mu_E$ , blue), the mean relative slice energy spread (red), and bunch chirp ( $h$ , purple).

the power gain length,  $\lambda_u$  the undulator period,  $\sigma_r$  the transverse bunch size, and  $\lambda_R$  is the FEL wavelength. For the bunches in Fig. 4, the most stringent of these conditions is found to be (iii), and hence the range of possible FEL wavelengths satisfies  $\lambda_R \gtrsim 4\pi\epsilon_{\perp} \approx 6 \text{ nm}$ .

Alternatively, the large energy chirp generated during acceleration could instead be used to compress the bunch to sub-fs duration, resulting in high ( $\gtrsim 10 \text{ kA}$ ) peak currents — we note that similar electron bunch parameters were recently assumed in a proposed scheme for generating high peak power, attosecond-duration soft x-rays [57].

In summary, we have demonstrated a simple scheme to inject electrons directly into the wakefield driven by a drive pulse guided by an all-optical plasma channel. We used this approach to generate dark-current-free bunches of energy  $1.2 \text{ GeV}$  and  $4.5\%$  relative energy spread with  $120 \text{ TW}$  laser pulses guided in a  $110 \text{ mm}$ -long HOFI plasma channel. Our measurements, confirmed by PIC simulations, showed that high-quality electron bunches were only obtained when the drive pulse was well aligned with the channel axis and focused close to the density down-ramp formed at the channel entrance. In contrast, bunches injected via ionization had much higher energy spread, and were found to occur preferentially when the drive was misaligned with the channel. Start-to-end simulations of the channel formation, and electron injection and acceleration showed that increasing the channel length to  $L_d \approx 410 \text{ mm}$  would yield  $3.65 \text{ GeV}$  bunches, with a slice relative energy spread below the per-mille level.

This experiment is the first to exploit sculpting of the longitudinal and transverse density profile of all-optical plasma channels to control electron injection into a plasma channel accelerator stage. The use of additional

laser pulses, plus further tailoring of the gas density prior to formation of the HOFI channel, can be expected to provide additional control. We note that HOFI channels have been operated at repetition rates in the kilohertz range [38], and new techniques have been developed for driving GeV-scale plasma accelerator stages with few-joule, few-kHz thin-disc lasers [58, 59]. These advances, and those reported here, show promise for the development of high-repetition-rate compact radiation sources, including FELs.

The authors would like to acknowledge useful discussions with Rémi Lehe. This work was supported by the UK Science and Technology Facilities Council (STFC UK) [grant numbers ST/R505006/1, ST/S505833/1 & ST/V001655/1]; the Engineering and Physical Sciences Research Council [grant numbers EP/R513295/1 & EP/V006797/1]; and the Central Laser Facility of the United Kingdom. This material is based upon work supported by the Air Force Office of Scientific Research under award number FA9550-18-1-7005. Computing resources provided by STFC Scientific Computing Department's SCARF cluster. The CFD work used in this study was supported by funding from the CLF/EPAC (Extreme Photonics Applications Centre). The software used in this work was developed in part by the DOE NNSA- and DOE Office of Science- supported Flash Center for Computational Science at the University of Chicago and the University of Rochester.

This research was funded in whole, or in part, by EPSRC and STFC, which are Plan S funders. For the purpose of Open Access, the author has applied a CC BY public copyright licence to any Author Accepted Manuscript version arising from this submission.

- 
- \* apicksley@lbl.gov; Present address: Lawrence Berkeley National Laboratory, Berkeley, California 94720, USA
- [1] T. Tajima and J. M. Dawson, *Physical Review Letters* **43**, 267 (1979).
  - [2] J. Van Tilborg, C. Schroeder, C. Filip, C. Tóth, C. Geddes, G. Fubiani, R. Huber, R. Kaindl, E. Esarey, and W. Leemans, *Physical Review Letters* **96**, 014801 (2006).
  - [3] T. Ohkubo, A. Maekawa, R. Tsujii, T. Hosokai, K. Kinoshita, K. Kobayashi, M. Uesaka, A. Zhidkov, K. Nemoto, Y. Kondo, and Y. Shibata, *Physical Review Special Topics-Accelerators And Beams* **10**, 031301 (2007-03).
  - [4] A. D. Debus, M. Bussmann, U. Schramm, R. Sauerbrey, C. D. Murphy, Z. Major, R. Hörlein, L. Veisz, K. Schmid, J. Schreiber, K. Witte, S. P. Jamison, J. G. Gallacher, D. A. Jaroszynski, M. C. Kaluza, B. Hidding, S. Kiselev, R. Heathcote, P. S. Foster, D. Neely, E. J. Divall, C. J. Hooker, J. M. Smith, K. Ertel, A. J. Langley, P. Norreys, J. L. Collier, and S. Karsch, *Physical Review Letters* **104**, 084802 (2010).
  - [5] O. Lundh, J. Lim, C. Rechatin, L. Ammoura, A. Ben-Ismaïl, X. Davoine, G. Gallot, J. P. Goddet, E. Lefebvre, V. Malka, and J. Faure, *Nature Physics* **7**, 219 (2011).
  - [6] M. Heigoldt, A. Popp, K. Khrennikov, J. Wenz, S.-W. Chou, S. Karsch, S. I. Bajlekov, S. M. Hooker, and B. Schmidt, *Physical Review Special Topics-Accelerators And Beams* **18**, 121302 (2015).
  - [7] W. P. Leemans, B. Nagler, A. J. Gonsalves, C. Tóth, K. Nakamura, C. G. R. Geddes, E. Esarey, C. B. Schroeder, and S. M. Hooker, *Nature Physics* **2**, 696 (2006).
  - [8] S. Karsch, J. Osterhoff, A. Popp, T. P. Rowlands-Rees, Z. Major, M. Fuchs, B. Marx, R. Hörlein, K. Schmid, L. Veisz, S. Becker, U. Schramm, B. Hidding, G. Pretzler, D. Habs, F. Grüner, F. Krausz, and S. M. Hooker, *New Journal of Physics* **9**, 415 (2007).
  - [9] X. Wang, R. Zgadzaj, N. Fazel, Z. Li, S. A. Yi, X. Zhang, W. Henderson, Y. Y. Chang, R. Korzekwa, H. E. Tsai, C. H. Pai, H. Quevedo, G. Dyer, E. Gaul, M. Martinez, A. C. Bernstein, T. Borger, M. Spinks, M. Donovan, V. Khudik, G. Shvets, T. Ditmire, and M. C. Downer, *Nature Communications* **4** (2013), 10.1038/ncomms2988.
  - [10] W. P. Leemans, A. J. Gonsalves, H. S. Mao, K. Nakamura, C. Benedetti, C. B. Schroeder, C. Toth, J. Daniels, D. E. Mittelberger, S. S. Bulanov, J. L. Vay, C. G. R. Geddes, and E. Esarey, *Physical Review Letters* **113**, 245002 (2014).
  - [11] J. Shin, H. T. Kim, V. B. Pathak, C. Hojbota, S. K. Lee, J. H. Sung, H. W. Lee, J. W. Yoon, C. Jeon, K. Nakajima, F. Sylla, A. Lifschitz, E. Guillaume, C. Thauray, V. Malka, and C. H. Nam, *Plasma Physics and Controlled Fusion* **60**, 064007 (2018).
  - [12] A. J. Gonsalves, K. Nakamura, J. Daniels, C. Benedetti, C. Pieronek, T. C. De Raadt, S. Steinke, J. H. Bin, S. S. Bulanov, J. Van Tilborg, C. G. R. Geddes, C. B. Schroeder, C. Tóth, E. Esarey, K. Swanson, L. Fan-Chiang, G. Bagdasarov, N. Bobrova, V. Gasilov, G. Korn, P. Satorov, and W. P. Leemans, *Physical Review Letters* **122**, 84801 (2019).
  - [13] L. Ke, K. Feng, W. Wang, Z. Qin, C. Yu, Y. Wu, Y. Chen, R. Qi, Z. Zhang, Y. Xu, *et al.*, *Physical review letters* **126**, 214801 (2021).
  - [14] S. Corde, C. Thauray, A. Lifschitz, G. Lambert, K. Ta Phuoc, X. Davoine, R. Lehe, D. Douillet, A. Rousse, and V. Malka, *Nature Communications* **4** (2013), 10.1038/ncomms2528.
  - [15] F. Albert and A. G. Thomas, *Plasma Physics and Controlled Fusion* **58**, 103001 (2016).
  - [16] W. Wang, K. Feng, L. Ke, C. Yu, Y. Xu, R. Qi, Y. Chen, Z. Qin, Z. Zhang, M. Fang, J. Liu, K. Jiang, H. Wang, C. Wang, X. Yang, F. Wu, Y. Leng, J. Liu, R. Li, and Z. Xu, *Nature* **595**, 516 (2021).
  - [17] M. Labat, J. C. Cabadağ, A. Ghaith, A. Irman, A. Berlioux, P. Berteaud, F. Blache, S. Bock, F. Bouvet, F. Briquez, Y.-Y. Chang, S. Corde, A. Debus, C. D. Oliveira, J.-P. Duval, Y. Dietrich, M. E. Ajjouri, C. Eisenmann, J. Gautier, R. Gebhardt, S. Grams, U. Helbig, C. Herbeaux, N. Hubert, C. Kitegi, O. Kononenko, M. Kuntzsch, M. LaBerge, S. Lê, B. Leluan, A. Loulergue, V. Malka, F. Marteau, M. H. N. Guyen, D. Oumbarek-Espinos, R. Pausch, D. Pereira, T. Püschel, J.-P. Ricaud, P. Rommeluere, E. Roussel, P. Rousseau, S. Schöbel, M. Sebdaoui, K. Steiniger, K. Tavakoli, C. Thauray, P. Ufer, M. Valléau, M. Vandenberghe, J. Vétéran, U. Schramm, and M.-E. Couprie, *Nature Photonics* , 1 (2022).
  - [18] R. Pompili, D. Alesini, M. P. Anania, S. Arjmand, M. Behtouei, M. Bellaveglia, A. Biagioni, B. Buonomo, F. Cardelli, M. Carpanese, E. Chiadroni, A. Cianchi, G. Costa, A. D. Dotto, M. D. Giorno, F. Dipace, A. Doria, F. Filippi, M. Galletti, L. Giannessi, A. Giribono, P. Iovine, V. Lollo, A. Mostacci, F. Nguyen, M. Opromolla, E. D. Palma, L. Pellegrino, A. Petralia, V. Petrillo, L. Piersanti, G. D. Pirro, S. Romeo, A. R. Rossi, J. Scifo, A. Selce, V. Shpakov, A. Stella, C. Vaccarezza, F. Villa, A. Zigler, and M. Ferrario, *Nature* **605**, 659 (2022).
  - [19] M. Galletti, D. Alesini, M. P. Anania, S. Arjmand, M. Behtouei, M. Bellaveglia, A. Biagioni, B. Buonomo, F. Cardelli, M. Carpanese, E. Chiadroni, A. Cianchi, G. Costa, A. D. Dotto, M. D. Giorno, F. Dipace, A. Doria, F. Filippi, G. Franzini, L. Giannessi, A. Giribono, P. Iovine, V. Lollo, A. Mostacci, F. Nguyen, M. Opromolla, L. Pellegrino, A. Petralia, V. Petrillo, L. Piersanti, G. D. Pirro, R. Pompili, S. Romeo, A. R. Rossi, A. Selce, V. Shpakov, A. Stella, C. Vaccarezza, F. Villa, A. Zigler, and M. Ferrario, *Physical Review Letters* **129**, 234801 (2022).
  - [20] M. Fuchs, R. Weingartner, A. Popp, Z. Major, S. Becker, J. Osterhoff, I. Cortrie, B. Zeitler, R. Hörlein, G. D. Tsakiris, U. Schramm, T. P. Rowlands-Rees, S. M. Hooker, D. Habs, F. Krausz, S. Karsch, and F. Grüner, *Nature Physics* **5**, 826 (2009).
  - [21] S. Kneip, C. McGuffey, J. L. Martins, S. F. Martins, C. Bellei, V. Chvykov, F. Dollar, R. Fonseca, C. Huntington, G. Kalintchenko, A. Maksimchuk, S. P. D. Mangles, T. Matsuoka, S. R. Nagel, C. A. J. Palmer, J. Schreiber, K. T. Phuoc, A. G. R. Thomas, V. Yanovsky, L. O. Silva, K. Krushelnick, and Z. Najmudin, *Nature Physics* **6**, 980 (2010).
  - [22] K. T. Phuoc, S. Corde, C. Thauray, V. Malka, A. Tafzi, J.-P. Goddet, R. C. Shah, S. Sebban, and A. Rousse, *Nature Photonics* **6**, 308 (2012).
  - [23] N. D. Powers, I. Ghebregziabher, G. Golovin, C. Liu, S. Chen, S. Banerjee, J. Zhang, and D. P. Umstadter, *Nature Publishing Group* **8**, 28 (2013).

- [24] K. Khrennikov, J. Wenz, A. Buck, J. Xu, M. Heigoldt, L. Veisz, and S. Karsch, *Physical Review Letters* **114**, 195003 (2015).
- [25] E. Esarey, C. B. Schroeder, and W. P. Leemans, *Reviews of Modern Physics* **81**, 1229 (2009-08).
- [26] A. Gonsalves, B. Pollock, and W. Lu, *AIP Conference Proceedings* **1812**, 030001 (2017).
- [27] R. Shalloo, *Hydrodynamic optical-field-ionized plasma waveguides for laser plasma accelerators*, Ph.D. thesis, University of Oxford (2018).
- [28] R. J. Shalloo, C. Arran, L. Corner, J. Holloway, J. Jonnerby, R. Walczak, H. M. Milchberg, and S. M. Hooker, *Physical Review E* **97**, 053203 (2018), arXiv:1801.00695.
- [29] R. J. Shalloo, C. Arran, A. Picksley, A. V. Boetticher, L. Corner, J. Holloway, G. Hine, J. Jonnerby, H. M. Milchberg, C. Thornton, R. Walczak, and S. M. Hooker, *Physical Review Accelerators and Beams* **22**, 41302 (2019).
- [30] C. G. Durfee and H. M. Milchberg, *Physical Review Letters* **71**, 2409 (1993).
- [31] C. G. Durfee, F. Lynch, and H. M. Milchberg, *Optics Letters* **20**, 946 (1995).
- [32] T. R. Clark and H. M. Milchberg, *Physical Review Letters* **78**, 2373 (1997).
- [33] V. Kumarappan, K. Y. Kim, and H. M. Milchberg, *Physical Review Letters* **94**, 205004 (2005).
- [34] A. Picksley, A. Alejo, R. J. Shalloo, C. Arran, A. von Boetticher, L. Corner, J. A. Holloway, J. Jonnerby, O. Jakobsson, C. Thornton, R. Walczak, and S. M. Hooker, *Physical Review E* **102**, 53201 (2020), arXiv:2008.13683.
- [35] A. Picksley, A. Alejo, J. Cowley, N. Bourgeois, L. Corner, L. Feder, J. Holloway, H. Jones, J. Jonnerby, H. M. Milchberg, L. R. Reid, A. J. Ross, R. Walczak, and S. M. Hooker, *Physical Review Accelerators and Beams* **23**, 81303 (2020), arXiv:2006.00810.
- [36] B. Miao, L. Feder, J. E. Shrock, A. Goffin, and H. M. Milchberg, *Physical Review Letters* **125**, 74801 (2020).
- [37] L. Feder, B. Miao, J. E. Shrock, A. Goffin, and H. M. Milchberg, *Physical Review Research* **2**, 43173 (2020), arXiv:2008.06771.
- [38] A. Alejo, J. Cowley, A. Picksley, R. Walczak, and S. Hooker, *Physical Review Accelerators and Beams* **25**, 011301 (2022).
- [39] R. H. H. Scott, N. Bourgeois, C. Thornton, J. Cowley, W. Rittershofer, T. Klein, J. Osterhoff, D. R. Symes, C. Hooker, and S. M. Hooker, *Physical Review Accelerators and Beams* **23**, 111301 (2020).
- [40] K. Oubrierie, A. Leblanc, O. Kononenko, R. Lahaye, I. A. Andriyash, J. Gautier, J.-P. Goddet, L. Martelli, A. Tafzi, K. Ta Phuoc, *et al.*, *Light: Science & Applications* **11**, 1 (2022).
- [41] B. Miao, J. Shrock, L. Feder, R. Hollinger, J. Morrison, R. Nedbailo, A. Picksley, H. Song, S. Wang, J. Rocca, *et al.*, *Physical Review X* **12**, 031038 (2022).
- [42] F. M. Foerster, A. Döpp, F. Haberstroh, K. v. Grafenstein, D. Campbell, Y.-Y. Chang, S. Corde, J. P. Couperus Cabadağ, A. Debus, M. F. Gilljohann, A. F. Habib, T. Heinemann, B. Hidding, A. Irman, F. Irshad, A. Knetsch, O. Kononenko, A. Martinez de la Ossa, A. Nuttner, R. Pausch, G. Schilling, A. Schletter, S. Schöbel, U. Schramm, E. Travac, P. Ufer, and S. Karsch, *Phys. Rev. X* **12**, 041016 (2022).
- [43] K. v. Grafenstein, F. Foerster, F. Haberstroh, D. Campbell, F. Irshad, F. Salgado, G. Schilling, E. Travac, N. Weiße, M. Zepf, *et al.*, *Scientific Reports* **13**, 11680 (2023).
- [44] C. Aniculaesei, H. T. Kim, B. J. Yoo, K. H. Oh, and C. H. Nam, *Review of Scientific Instruments* **89**, 025110 (2018).
- [45] “See Supplemental Material for further details of the laser guiding, electron diagnostics and the numerical simulations, which includes Refs. [60–66].”
- [46] G. J. Hutchens, *Journal of Applied Physics* **88**, 3654 (2000).
- [47] H. Suk, N. Barov, J. B. Rosenzweig, and E. Esarey, *Physical Review Letters* **86**, 1011 (2001).
- [48] K. Schmid, A. Buck, C. M. S. Sears, J. M. Mikhailova, R. Tautz, D. Herrmann, M. Geissler, F. Krausz, and L. Veisz, *Physical Review Special Topics - Accelerators and Beams* **13**, 091301 (2010).
- [49] A. Buck, J. Wenz, J. Xu, K. Khrennikov, K. Schmid, M. Heigoldt, J. M. Mikhailova, M. Geissler, B. Shen, F. Krausz, S. Karsch, and L. Veisz, *Physical Review Letters* **110**, 185006 (2013).
- [50] S. Bulanov, N. Naumova, F. Pegoraro, and J. Sakai, *Physical Review E* **58**, R5257 (1998).
- [51] T. D. Arber, K. Bennett, C. S. Brady, A. Lawrence-Douglas, M. G. Ramsay, N. J. Sircombe, P. Gillies, R. G. Evans, H. Schmitz, A. R. Bell, and C. P. Ridgers, *Plasma Physics and Controlled Fusion* **57**, 113001 (2015).
- [52] B. Fryxell, K. Olson, P. Ricker, F. X. Timmes, M. Zingale, D. Q. Lamb, P. MacNeice, R. Rosner, J. W. Truran, and H. Tufo, *The Astrophysical Journal Supplement Series* **131**, 273 (2000).
- [53] R. Lehe, M. Kirchen, I. A. Andriyash, B. B. Godfrey, and J. L. Vay, *Computer Physics Communications* **203**, 66 (2016), arXiv:1507.04790.
- [54] A. Döpp, C. Thauray, E. Guillaume, F. Massimo, A. Lifschitz, I. Andriyash, J.-P. Goddet, A. Tafzi, K. Ta Phuoc, and V. Malka, *Physical Review Letters* **121**, 074802 (2018).
- [55] R. D’Arcy, S. Wesch, A. Aschikhin, S. Bohlen, C. Behrens, M. J. Garland, L. Goldberg, P. Gonzalez, A. Knetsch, V. Libov, *et al.*, *Physical review letters* **122**, 034801 (2019).
- [56] Z. Huang and K.-J. Kim, *Physical Review Special Topics - Accelerators and Beams* **10**, 034801 (2007).
- [57] C. Emma, X. Xu, A. Fisher, R. Robles, J. MacArthur, J. Cryan, M. Hogan, P. Musumeci, G. White, and A. Marinelli, *APL Photonics* **6** (2021).
- [58] O. Jakobsson, S. M. Hooker, and R. Walczak, *Physical Review Letters* **127**, 184801 (2021).
- [59] J. J. van de Wetering, S. M. Hooker, and R. Walczak, *Phys. Rev. E* **108**, 015204 (2023).
- [60] Y. Fournier, J. Bonelle, C. Moulinec, Z. Shang, A. Sunderland, and J. Uribe, *Computers & Fluids* **45**, 103 (2011), 22nd International Conference on Parallel Computational Fluid Dynamics (ParCFD 2010).
- [61] “code\_saturne,” <https://www.code-saturne.org/cms/web/>, accessed: 2023-07-24.
- [62] A. Popp, J. Vieira, J. Osterhoff, Z. Major, R. Hörlein, M. Fuchs, R. Weingartner, T. P. Rowlands-Rees, M. Marti, R. A. Fonseca, S. F. Martins, L. O. Silva, S. M. Hooker, F. Krausz, F. Grüner, and S. Karsch, *Phys. Rev. Lett.* **105**, 215001 (2010).
- [63] S. Jalas, I. Dornmair, R. Lehe, H. Vincenti, J.-L. Vay, M. Kirchen, and A. R. Maier, *Physics of Plasmas* **24**,

- 033115 (2017).
- [64] M. Kirchen, R. Lehe, B. B. Godfrey, I. Dornmair, S. Jalas, K. Peters, J.-L. Vay, and A. R. Maier, *Physics of Plasmas* **23**, 100704 (2016).
- [65] M. Kirchen, R. Lehe, S. Jalas, O. Shapoval, J.-L. Vay, and A. R. Maier, *Phys. Rev. E* **102**, 013202 (2020).

- [66] A. Huebl, R. Lehe, J.-L. Vay, D. P. Grote, I. Sbalzarini, S. Kuschel, D. Sagan, F. Pérez, F. Koller, and M. Bussmann, “openPMD: A meta data standard for particle and mesh based data,” <https://github.com/openPMD> (2015).

## SUPPLEMENTAL MATERIAL

In this Supplemental Information we provide further details of the laser guiding and electron energy diagnostics, the hybrid jet-cell target, and the start-to-end simulations.

### DIAGNOSING GUIDING

#### On-shot far-field monitor calibration

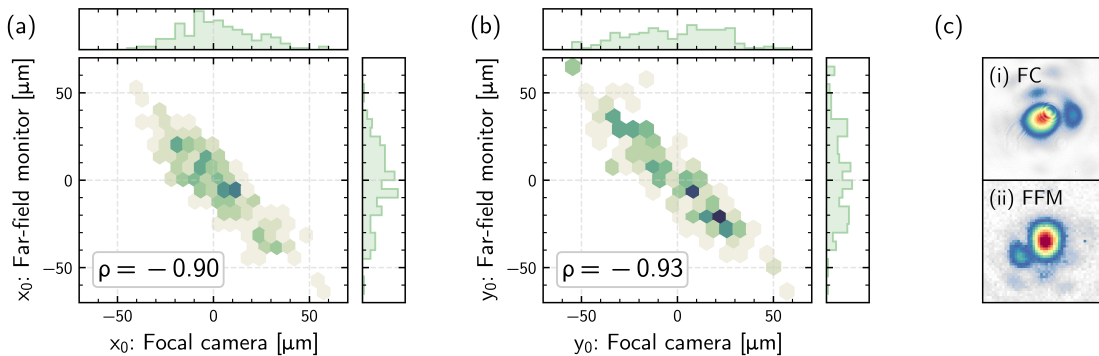


Fig. S1. Correlation between the centroid position of the focal spot measured by a camera placed at the focus (Focal camera, FC) and via a small portion of the beam transmitted through the final turning mirror (Far-field monitor, FFM) in the (a) horizontal and (b) vertical directions. Pearson’s correlation coefficients of  $\rho = -0.90$  (horizontal) and  $\rho = -0.93$  (vertical) were measured, indicating strong correlations between the two cameras and hence validity of this diagnostic as a proxy for the position of the drive pulse at focus. (c) Example images of the same focus recorded on (i) FC and (ii) FFM looking at a  $\pm 120 \mu\text{m}$  region around the identified centroid.

Calibration of the on-shot far-field monitor (FFM) was performed by simultaneously recording images of the foci of both the leakage beam and the main drive pulse on two separate cameras; the “FFM” and “Focal” cameras respectively. The FFM utilized the  $< 1\%$  transmitted component from the final turning mirror before the interaction (*after* the focusing optic) and hence shared a common path with the main beam up until this point, minimising possible sources of uncorrelated fluctuations. The calibration dataset consisted of 192 shots taken in a low-power mode at 0.05 Hz, matching the repetition-rate of the full-power beam. Figure S1 shows the correlations between the (a) horizontal and (b) vertical focal spot centroids on the two cameras. The leakage-to-main beam Pearson’s correlation coefficient was calculated to be  $-0.90$  and  $-0.93$  in the horizontal and vertical directions respectively, indicating strong (negative) correlation between the two (the sign of the correlation arising from the relative orientation of the CCDs). Example images of the same focus measured on both cameras are shown in Fig. S1(c).

Ellipses can be fitted to the distributions shown in Fig. S1(a) and (b), with the length of the minor axes representing an average measure of the uncertainty of the true focus position as measured by the FFM. Therefore, an estimate of the uncertainty of a single measurement of the radial offset with respect to the axis of the guiding channel is a summation in quadrature of these values combined with the measured spatial jitter of the axicon focus, corresponding to an overall uncertainty of  $9.1 \mu\text{m}$ . For this reason,  $10 \mu\text{m}$ -wide bins are used throughout this work when studying the interaction as a function of the radial input offset.

### Characterisation of well-guided shots

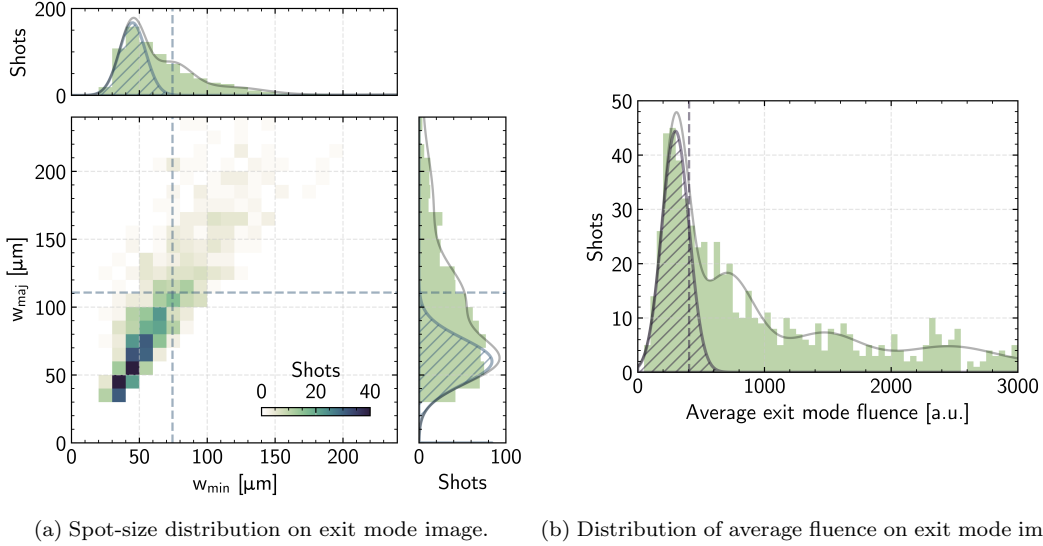


Fig. S2. Measured distributions of (a) spot-size and (b) average fluence within the automatically-identified ROI on exit mode images. Each distribution is fitted with a Gaussian Mixture Model (grey curve), with the dominant contribution represented by the shaded region. The thresholds used to identify well-guided events are represented by the dashed lines.

The distribution of the drive beam energy at the exit of the guiding channel was imaged on every shot by the exit mode imaging system described in the main text. A region of interest (ROI) in each image is automatically identified by finding the largest contour within the image that contained pixels with values above  $(1/e) \times$  the 99<sup>th</sup>-percentile of the pixel counts. The distribution of light belonging to the guided mode is identified by fitting an ellipse to this contour, and applying a mask to the image around its centre-of-mass of size three times the fitted ellipse in order to isolate the signal from the guided mode. The  $D4\sigma$ -method is then used to calculate the minor and major spot-sizes ( $w_{\min}$  and  $w_{\max}$ ) of the guided mode within the masked image. The average pixel count contained within the identified spot ( $\mu_{\text{fluence}}$ ) is also recorded.

Well-guided events are characterised by guided modes with a combination of small spot-sizes and high fluence on the exit mode imager, since this indicates minimal evolution during propagation with high throughput from the channel. The thresholds for these requirements were found by applying Gaussian Mixture Models (GMMs) to the measured distributions of  $w_{\min}$ ,  $w_{\max}$  and  $\mu_{\text{fluence}}$  to estimate the dominant contribution, as demonstrated by the hatched, shaded regions in the distributions in Fig. S2. The number of Gaussian peaks within the GMM,  $n$ , was allowed to vary between 1 and 6 for each distribution, with the best fit value for  $n$  selected using the Akaike information criterion that includes both a goodness-of-fit measure and a preference for fewer components (smaller  $n$ ) to avoid over-fitting. For the spot-size measurements [Fig. S2(a)], this dominant contribution — centred around the lowest measured values of  $w_{\min}$  and  $w_{\max}$  — corresponds to well-guided shots, with spot-sizes comparable to the input drive beam spot-size ( $\sim 40 \mu\text{m}$ ). It should be noted that images of the guided mode on the exit mode imager included a non-constant background contribution from scattered axicon light, leading to measured spot-sizes that often exceeded direct measurements of the input drive beam focus where this effect was not present. The dominant contribution to the distribution of the average exit mode fluence [Fig. S2(b)] instead corresponds to poorly-guided events, with minimal intensity within the identified region of interest mainly as a result of scattered light from the axicon beam. Thresholds for well-guided shots were defined using the fitted mean and width of these dominant contributions, resulting in the following requirements for a shot to be considered “well-guided”:

- $w_{\min} \leq 72 \mu\text{m}$ ,
- $w_{\max} \leq 110 \mu\text{m}$ ,
- $\mu_{\text{fluence}} \geq 410$  counts.

These requirements typically led to approximately 50% of all events being characterised as well-guided.

## GAS TARGET LONGITUDINAL UNIFORMITY

### Simulations

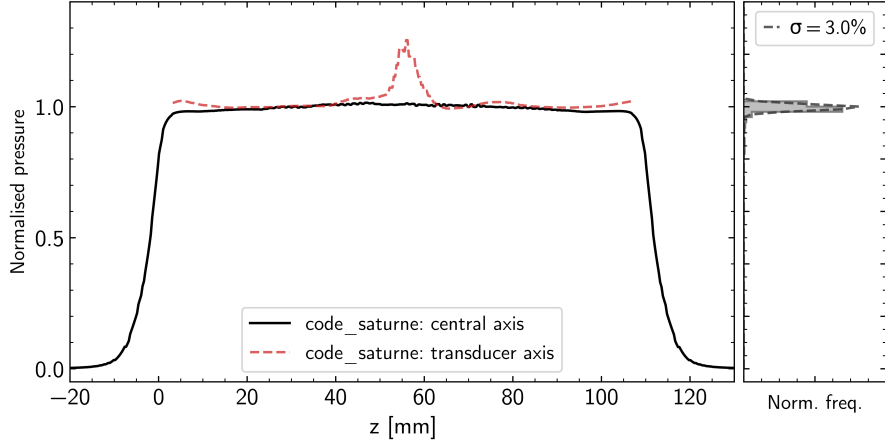


Fig. S3. Left: Normalised steady-state pressure profile from CFD simulations of the gas target. The simulated pressure profile includes a localised pressure spike around the centre of target along its top surface (“transducer axis” — red, dashed) which was observed via measurements with pressure transducers. Right: Histogram of the simulated normalised gas pressure along the central axis of the target, indicating relative longitudinal pressure variations of 3.0% RMS.

Computational fluid dynamics (CFD) simulations of hydrogen gas flow within the gas target were performed using the open source software `code_saturne` [60, 61]. The simulations were performed by members of the Scientific Computing Department, STFC Daresbury Laboratory. The gas inlet, central chamber of the target and entrance and exit pinholes were reproduced in simulation, with hydrogen gas flowed into the target at a backing pressure of 1.0 bar. The simulations indicated that a steady state was reached approximately 22 ms after the valve opened. As shown in Fig. S3, during steady-state the simulations predicted that along the central axis of the target — the laser propagation axis — the gas pressure is uniform to within 3% RMS between  $z = 4 - 106$  mm. Experimental verification of the longitudinal pressure profile along the central axis could not be undertaken in-situ at RAL, and hence a separate measurement campaign was performed, as discussed in the following section.

In the experiments performed at RAL, two independently-calibrated gas pressure transducers (type: RS-PRO 797-4983) were connected to the upper surface of the target volume to measure the absolute gas pressure, and its evolution, within the target on every shot. One transducer was located near the centre of the target ( $z = 59$  mm), while the other was located towards the front ( $z = 29$  mm). The CFD simulations predicted that the gas pressure distribution at the top of the target — along the axis measured by the pressure transducers — featured a small ( $\sim 5$  mm) region around the centre, directly above the gas inlet, where the pressure increased by approximately 30% [see Fig. S3]. This pressure bump was observed in the experiment, since the centre transducer measured pressures that were  $(27 \pm 1)\%$  higher than the transducer towards the front, consistent over fill pressures ranging from 20 mbar to 170 mbar.

### Measurement of gas pressure uniformity along laser axis

The uniformity of the longitudinal gas pressure profile along the central axis of the gas target was measured at the Oxford Plasma Accelerator Laboratory (OPAL) using the plasma fluorescence technique discussed in Ref. [41]. To do this, an extended hydrogen plasma column was formed by focusing a  $(120 \pm 4)$  mJ, 45 fs laser pulse with the same axicon used in the experiments at RAL (approach angle  $1.6^\circ$ ). The RMS spatial jitter of the axicon focus along the length of the target was measured to be  $0.45 \mu\text{m} \times 0.44 \mu\text{m}$  ( $x \times y$ ). Fluorescence light emitted from this plasma was imaged transversely on to a 16-bit CMOS sensor (Andor Xyla 5.5, 10 ms exposure time) through a window on top of the gas target. This window allowed viewing access to the longitudinal region extending from  $z = 17 - 105$  mm within the 110 mm-long target, as shown in Fig. S4(b). A bandpass filter centered on  $(656 \pm 10)$  nm was placed in front of the sensor to isolate the hydrogen-alpha fluorescence.

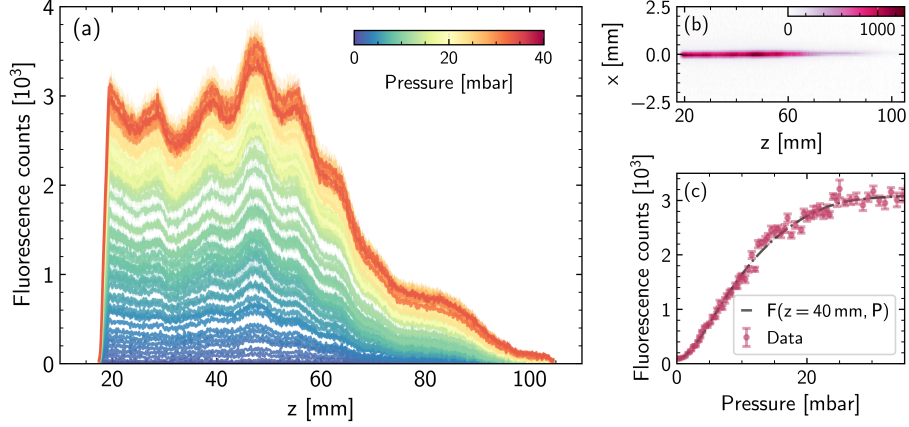


Fig. S4. (a) Calibration dataset demonstrating the measured plasma fluorescence along the gas target as a function of backfill pressure. (b) Example (false-colour) raw fluorescence image of the axicon-generated hydrogen plasma at OPAL. (c) An example of a calibration curve,  $F(z = 40 \text{ mm}, P)$ , demonstrating the polynomial fit used to extract the relationship between measured fluorescence intensity and gas pressure.

Firstly, a calibration dataset was taken that allowed the relation between the measured plasma fluorescence along the target and the gas pressure to be determined. This involved uniformly filling the gas target (and entire target chamber) with hydrogen gas over pressures ranging from  $P = 0.3 \text{ mbar}$  to  $34 \text{ mbar}$ . The fluorescence produced by the plasma column generated by the axicon focus within the hydrogen backfill was then captured by the imaging setup as a function of the longitudinal position along the target,  $z$ , as demonstrated in Fig. S4(a). The average measured fluorescence of ten shots, integrated over the transverse axis, was then fit to a seventh-order polynomial to produce a relation between the light intensity and the gas pressure,  $F(z, P)$ , at each longitudinal position within the cell. The uncertainty on the fit includes contributions from, and is dominated by, the shot-to-shot fluctuations in the measured plasma fluorescence during backfill operation, which were typically on the order of 15%. An example of this fit for  $z = 40 \text{ mm}$  is shown in Fig. S4(c). These calibration curves could then be used to infer the gas pressure along the target by measuring the plasma fluorescence when pulsing gas into the cell.

The target chamber was then evacuated and the gas target was operated in a pulsed mode, using the same valve opening time (150 ms), backing pressure (1.0 bar) and relative laser arrival time ( $\Delta t = 146 \text{ ms}$ ) as used in the main experiment at RAL. Again, ten events were recorded, with the measured fluorescence signal averaged. The gas pressure along the central axis of the target could then be extracted by inverting the calibration curves and relating the measured fluorescence in pulsed operation,  $f(z)$ , to the longitudinal gas pressure,  $P(z)$ . The gas target was kept in place in both the backfill and pulsed operation measurements to ensure that any modification of the axicon focus by the pinhole at the front of the target was consistent for both datasets.

The results of such a measurement are shown in Fig. S5. The lower axis shows the average fluorescence counts measured in pulsed operation mode. The upper, central plot compares the (normalised) measured longitudinal pressure along the central axis, reconstructed via inversion of the calibration functions, to that predicted by the CFD simulation. Good agreement between the two datasets can be seen, with a reduced chi-squared statistic of  $\chi_r^2 = 1.16$  indicating that the measurement was consistent with simulations of the longitudinal pressure along the central axis of the target. The measured relative RMS gas pressure variation along the target was found to be only 4.1% within the region accessible to the measurement ( $z = 17 - 105 \text{ mm}$ , approximately 80% of the length of the target), and very similar to the 3% RMS variations predicted by CFD simulations.

The total uncertainty on the reconstructed pressure at each longitudinal position includes contributions from the uncertainty on the polynomial fit to the calibration curves combined with the shot-to-shot fluctuations of the plasma fluorescence measured in pulsed operation mode. The relative uncertainty on the measurement grew along  $z$  as the focus generated at the far end of the target corresponds to light at the outer edges of the near-field laser profile on the axicon, and hence was more susceptible to laser energy and pointing jitters. In addition, the fluorescence signal in this region was significantly dimmer, reducing the signal-to-noise ratio and increasing the fit uncertainty in the calibration data, as can be seen in Fig. S4. The relative fluctuation in the measured fluorescence profile in pulsed operation mode was typically on the order of 15%, similar to backfill operation, and indicates that no further

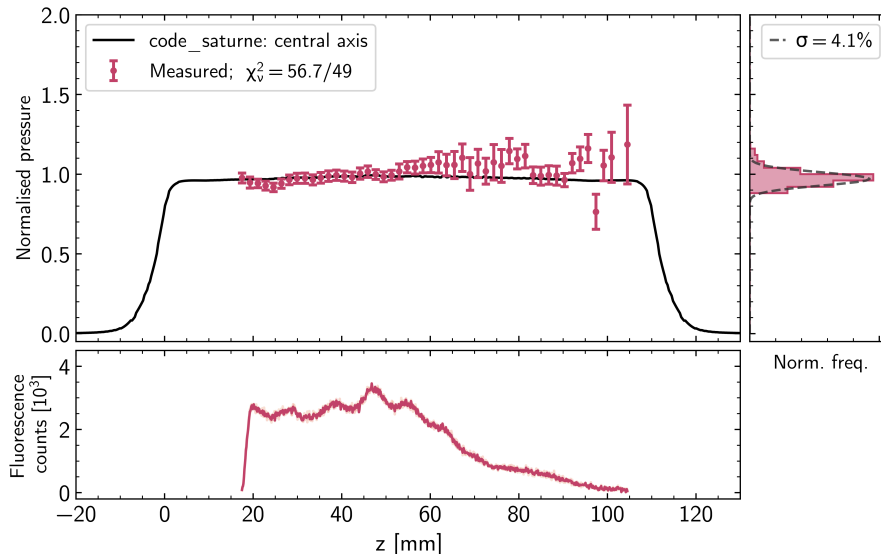


Fig. S5. Upper: Comparison of the normalised simulated longitudinal gas pressure profile (black, solid) and that measured experimentally (red) along the propagation axis of the laser. Lower: average plasma fluorescence counts measured during pulsed operation. Right: histogram of the measured normalised gas pressure, indicating relative longitudinal pressure variations of 4.1% RMS.

significant fluctuations were introduced in pulsed operation mode. The dominant contribution to the shot-to-shot fluctuations observed during these measurements was therefore consistent for both datasets and was likely a result of the laser energy jitter, measured to be 3.5% RMS.

## ELECTRON ENERGY UNCERTAINTY

The electron bunch spectral distribution was measured by dispersing the beam using a series of two 30 cm-long permanent dipole magnets located 0.59 m downstream of the exit pinhole, each with magnetic field strength of  $(1.01 \pm 0.01)$  T and longitudinally separated by 5 cm. The beams were vertically dispersed on to two scintillating screens (type: Lanex Regular), the surfaces of which were imaged onto two 16-bit CMOS detectors (type: Andor Neo 5.5). The combined height of the scintillating screens enabled measurement of electron energies ranging from 350 MeV to 3 GeV while simultaneously imaging the guided mode of the drive pulse. The scintillating screens provided a charge-dependent scintillation signal, calibrated via consideration of the collection efficiency of the imaging setup in combination with well-known properties of scintillating screens, resulting in an overall charge uncertainty of 26%.

A vertical array of eleven 145  $\mu\text{m}$ -thick fiducial tungsten wires was placed 1.86 m downstream of the exit of the second dipole to cast identifying shadows in the scintillation signal. The positions of these shadows could be used to reconstruct the trajectories of accelerated electrons and minimise the electron-beam-pointing uncertainty [9]. The main additional contribution to the energy uncertainty arises from uncertainties in the positions of the electron spectrometer components and the accuracy of the measured dipole field maps.

To quantify the relative contributions of these uncertainties, the electron propagation through the electron spectrometer was solved numerically for different electron energies (e.g. Fig. S6(a)), allowing comparison between the reconstructed energy of electrons on the scintillating screen and their true energy. The relative positions of all beam-line components after the gas target were allowed to vary in both  $y$  and  $z$  within the experimentally-determined uncertainty ( $\pm 1$  mm) with the field map amplitudes also randomly varied according to their measurement accuracy ( $\pm 1\%$ ). The resulting contributions to the energy uncertainty were then combined in quadrature to estimate the total energy-dependent systematic uncertainty, shown in Fig. S6(b).

The advantage of employing two consecutive dipoles, rather than a single magnet, is clear from Fig. S6(b). For a single magnet, the relative uncertainty scaled linearly with the electron energy, increasing from  $\sim 2\%$  at 0.3 GeV — the minimum energy that could be measured on the scintillating screen — to approximately 11% at 2.0 GeV. In contrast, the systematic energy uncertainty was decreased when using two magnets as a result of the increased dispersion of

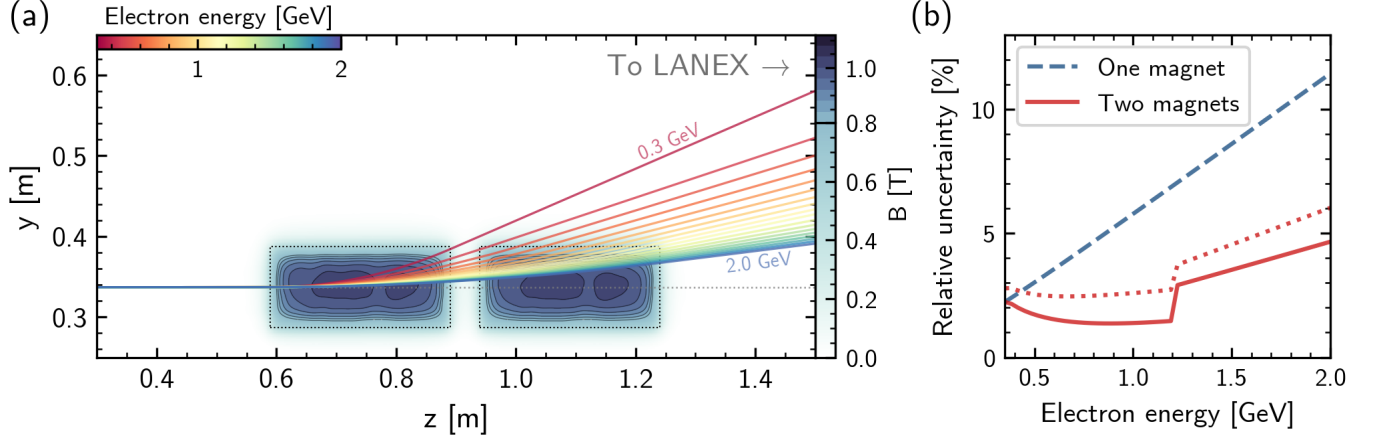


Fig. S6. (a) Measured electron spectrometer magnet field maps (blue) with field contours in the range  $0.8 \leq B_x \leq 1.1$  T ( $\Delta B_x = 0.04$  T) marked. Example electron trajectories are overlaid for energies between  $0.3 \leq E \leq 2.0$  GeV ( $\Delta E = 0.1$  GeV). (b) Relative uncertainty as a function of electron energy for one (blue, dashed) and two (red, solid) magnets. The increase in systematic uncertainty for two magnets without trajectory reconstruction is shown by the red, dotted line.

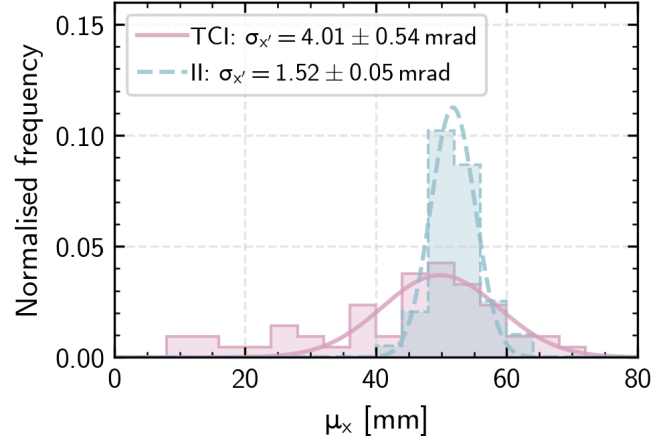


Fig. S7. Histogram of  $e^-$ -beam transverse position on ESPEC screen for well-guided shots. Shown in pink is the distribution for TCI ( $\Delta z = 0.8$  mm) and in blue is the distribution for II ( $\Delta z = -11.2$  mm). The width of the positional distributions (and their uncertainties) are converted into horizontal beam-pointing distributions via  $\sigma_{x'} = \sigma_x/z(E)$ , where  $z(E)$  represents the energy-dependent distance between the exit of the gas target and the position of the signal on the scintillating screen.

the beam. In this case, the relative energy uncertainty at 1.0 GeV was approximately 1%, with a discontinuity at  $\sim 1.2$  GeV created by electron trajectories exiting either the upper side of the second magnet or its far end. In both cases, the dominant contribution to the systematic uncertainties was the vertical position of the scintillating screen. As a result of the much reduced systematic energy uncertainty over the energies of interest, the two magnet setup was preferred.

For high-quality electron beams with low energy spread, as was typically observed in the TCI setup, no shadows from the fiducial wires were present within the electron spectra, which increases the systematic energy uncertainty. The additional energy uncertainty is dominated by uncertainties in the (vertical) beam pointing angle at the plasma exit as this results in changes of the position and angle of the beam as it enters the first dipole magnet.

The pointing angle of the electron beam as it exits the plasma can be affected by its relative betatron phase advance or the pulse-front tilt of the drive pulse [62]. While this could not be reconstructed on-shot for electron bunches that did not interact with the fiducial wires, the distribution of the pointing angle of all shots in the dataset can be estimated from the position of the transverse centroid of the electron bunches on the spectrometer scintillating screen. The results of this analysis are shown in Fig. S7 for the two injection schemes investigated in this study —

truncated-channel injection (TCI) in pink, and ionisation injection (II) in blue. Shown is a histogram of the transverse centroid position of electron bunches on the screen with respect to the left-edge of the screen (total width of 80 mm) for all well-guided shots in the datasets. The width of these centroid position distributions represents a measure of the shot-to-shot pointing angle fluctuations of the electron beam, multiplied by the energy-dependent distance between the exit of the plasma channel and the front surface of the scintillator screen. Gaussian fits to the distributions give pointing fluctuations of  $(4.01 \pm 0.54)$  mrad and  $(1.52 \pm 0.05)$  mrad for TCI and II respectively. This represents a direct measure of the horizontal electron beam pointing fluctuations which, on their own, do not significantly contribute to energy uncertainties as the electrons are dispersed vertically. However, laser-plasma accelerators are typically assumed to be cylindrically symmetric for many-cycle pulses, and hence the transverse beam-pointing fluctuations measured here would be expected to be representative of the magnitude of the vertical pointing fluctuations. It is hypothesised that the difference in horizontal pointing fluctuations between the two injection schemes are a result of the difference in injection location. For TCI, injection occurs at the channel entrance and therefore injected electrons will be more sensitive to the effect of slight transverse offsets and mis-matching of the laser pulse on subsequent propagation and acceleration within the channel.

The resulting increase in relative systematic energy uncertainty for the two magnet setup without trajectory reconstruction — assuming a vertical pointing fluctuation of 4 mrad — is shown in Fig. S6(b), represented by the dotted red line. At an energy of 1.0 GeV, the relative uncertainty increases from approximately 1% to close to 3%.

### START-TO-END SIMULATIONS

The timescales associated with the TCI scheme range from the femtosecond-scale for channel ionisation and electron injection, to multiple nanosecond scale for the truncated HOFI plasma channel expansion, and range from the micron scale for the density transition to the meter-scale for low-density propagation. A simulation that included all of the required physics over these time- and length-scales is beyond the capabilities of current particle-in-cell (PIC) codes. We therefore employed a chain of codes, as described below:

1. The fraction of electrons ionised, and initial electron momentum (through the process of OFI) was calculated using several separate particle-in-cell (PIC) simulations using the code `EPOCH` [51] in the two-dimensional geometry. The initial axicon line focus  $I_{\text{ax}}(r, z)$  was converted to an electron temperature distribution  $T_e(r, z)$  using these simulations as a look-up table. We have previously outlined details of the electron species thermalisation [28] in HOFI plasma channel expansion.
2. As described above, the initial gas density distribution  $n_{\text{gas}}(z)$  was separately determined via fluid simulations using the open source, computational fluid dynamics software `code_saturne` [61]. The steady state solution provided details of the length of the gas density plumes at the gas jet-cell entrance.
3.  $T_e(r, z)$  and  $n_{\text{gas}}(z)$  were input into the Eulerian magnetohydrodynamic code `FLASH` (v4.6.2) [52] on a three-dimensional  $(400 \times 400 \times 1000) \mu\text{m}^3$  grid, with adaptive-mesh-refinement used to dynamically resolve the fine-scale structure at the shock fronts. The simulation used a three-temperature model such that the electron, ion and radiation species could be independently evolved, with the electron and ion species also able to exchange heat. The energy diffusion and thermal conductivity modules were activated as this has previously been found to improve modelling of species propagation [34]. Tabulated values were used for the equation of state (EoS) and ionisation fraction of atomic  $H$ , along with the Rosseland and Planck opacities, with tables obtained from the `PROPACEOS` package. Radiation transport was modelled using multi-group diffusion, with a total of 6 energy groups distributed between 10 meV and 12 eV.
4. The calculated electron density  $n_e(r, z)$  and neutral density  $n_H(r, z)$  profiles after a time  $\Delta\tau$  were extracted from the `FLASH` simulation and input into `FBPIC` [53] — a PIC code that operates in the  $r$ - $z$  geometry. For the trapping section, simulations were run utilising the multi-GPU capabilities of `FBPIC` in the laboratory frame [63], and were propagated over 4 mm. The simulation window was  $600 \times 3500$  cells on the  $(r, z)$  cylindrical grid and co-propagated with the laser pulse. Electron and neutral species was initialised with  $3 \times 3 \times 8$  macro-particles in the  $r \times z \times \theta$  directions.
5. Since injection does not occur in the low-density HOFI plasma channel after the truncation section, it was possible to capture the physics of bunch acceleration using a boosted frame simulation with fewer macroparticles. This was necessary due to the length scales involved. Macroparticles from the laboratory simulation that made up the trapped bunch were isolated, and input into a second `FBPIC` simulation carried out with  $\gamma_{\text{boost}} = 12$

[64, 65], and  $1 \times 1 \times 8$  macro-particles in the  $r \times z \times \theta$  directions. Matched boundary layers with 128 damping cells were included transversely to account for light that leaked out of the plasma channel at an oblique angle. Simulation outputs were visualized using the open-PMD framework [66]. It should be noted that a single, long propagation, laboratory frame simulation was also carried out to confirm there were no additional contributions from ionisation injection during the meter-scale propagation section of the HOFI plasma channel.